Monte Carlo Simulations of Wave Scattering from Lossy Dielectric Random Rough Surfaces Using the Physics-Based Two-Grid Method and the Canonical-Grid Method

Qin Li, Chi Hou Chan, *Member, IEEE*, and Leung Tsang, *Fellow, IEEE*

***Abstract*—In using the method of moments to solve scattering by lossy dielectric surfaces, usually a single dense grid (SDG) with 30 points per wavelength is required for accurate results. A single coarse grid (SCG) of ten points per wavelength does not give accurate results. However, the central processing unit (CPU) and memory requirements of SDG are much larger than that of SCG. In a physics-based two-grid method (PBTG) two grids are used: a dense grid and a coarse grid. The method is based on the two observations: 1) Green's function of the lossy dielectric is attenuative and 2) the free-space Green's function is slowly varying on the dense grid. In this paper, the PBTG method is combined with the banded-matrix iterative approach/canonical grid method to solve rough surface scattering problem for both TE and TM cases and also for near grazing incidence. We studied cases of dielectric permittivities as high as $(25 + i)\varepsilon_0$ and incidence angle up to 85°. Salient features of the numerical results are: 1) an SCG has poorer accuracy for TM case than TE case; 2) PBTG-banded-matrix iterative approach/canonical grid BMIA/CAG method speeds up CPU and preserves the accuracy; it has an accuracy comparable to single dense grid and yet has CPU comparable to single coarse grid; 3) PBTG-BMIA/CAG gives accurate results for emissivity calculations and also for low grazing backscattering problems (LGBA); and 4) the computational complexity and the memory requirements of the present algorithm are $O(N \log(N))$ and $O(N)$, respectively, where N is the number of surface unknowns on the coarse grid.**

***Index Terms*—Grid generation, Monte Carlo methods, rough surfaces.**

I. Introduction

THE scattering of waves from random rough surfaces has been a topic of continued study for many years because of its broad applications. Recently, Monte Carlo simulations of the wave scattering problem have been a common approach because of the advent of modern computers and the development of fast numerical methods. Monte Carlo simulations performed by all authors require at least 20 wavelengths because the surface must have enough valleys and peaks to be a legitimate statistical sample (realization) in random rough surface simulations. The most common method that has been used in numerical simulations is the integral equation method [1]–[9]. Conventional implementation of the integral equation method requires an $O(N^3)$ operation and an $O(N^2)$ computer memory storage. Therefore, the simulation has been limited to small to moderate surface length with no more than a few thousand surface unknowns. Over the past few years, there are several fast numerical methods that have been developed [10]–[19]. One of them is the banded-matrix iterative approach/canonical grid method (BMIA/CAG) that permits the solution of large-scale random rough surface problems [13]–[19]. The essence of the method consists of decomposing the interaction into near and nonnear field interactions. The nonnear field interactions are then expanded on a canonical grid of a horizontal surface so that the fast Fourier transform (FFT) can be applied. The computational complexity and the memory requirements for BMIA/CAG are $O(N \log(N))$ and $O(N)$, respectively. Another method for the one-dimensional (1-D) case is by Michielssen's *et al.* [12], which has computational complexity of $O(N \log^2 N)$. For the case of perfectly electrical conductor (PEC), the paper by Michielssen *et al.* reports a central processing unit (CPU) of 8 to 12 min for 4000 unknowns while the BMIA/CAG method as reported in [17, Table II] reports a CPU of 20 min for 8000 unknowns. Thus, the two methods are comparable in CPU time for the PEC case. The BMIA/CAG is also applied to dielectric rough surface [19]. The experience with dielectric surface is that the CPU increases much more than the PEC case.

In the application of method of moments to rough surface scattering problem, a common implementation is to use a grid of ten points per wavelength to discretize the surface. We shall call such a gridding a single coarse grid (SCG). But, to study scattering by lossy dielectric rough surfaces with high permittivity, there can be rapid spatial variation of surface fields. Two alternatives were used. The first alternative is to use impedance boundary condition [20]. The disadvantage of this alternative is that an approximation is used in the problem without any error estimate. The second alternative is to use a dense grid with a large number of points (say

Manuscript received December 29, 1997; revised July 20, 1998. This work was supported in part by the National Science Foundation (ECS-9423861).

Q. Li and L. Tsang are with the Electromagnetics and Remote Sensing Laboratory, Department of Electrical Engineering, University of Washington, Seattle, WA 98195 USA.

C. H. Chan is with the Electromagnetics and Remote Sensing Laboratory, Department of Electrical Engineering, University of Washington, Seattle, WA 98195 USA, and with the Applied Electromagnetics Laboratory, Department of Electronic Engineering, City University of Hong Kong, Kowloon, Hong Kong.

Publisher Item Identifier S 0018-926X(99)03723-0.

more than 20 points) per wavelength. We shall call such a gridding a single dense grid (SDG). The disadvantage of this second alternative is that there is a large increase in CPU and required memory. The physics-based two-grid (PBTG) method [21] is an improvement over these two alternatives in that it has the same accuracy as the single dense grid and yet has CPU comparable with that of the single coarse grid. Another improvement is that the PBTG method can calculate the emissivity accurately because the method obeys energy conservation accurately. In PBTG, two grids were used: a dense grid and a sparse grid. The sparse grid is that of the usual ten points per wavelength. The dense grid ranges from 20 to higher number points per wavelength depending on the relative permittivity of the lossy dielectric medium. The key point of PBTG is based on the following two observations: 1) Green's function of the lossy dielectric is attenuative and 2) Green's function of free-space is slowly varying on the dense grid. Because of Kramer–Kronig relation, a large real part of dielectric constant is usually associated with a large imaginary part. The first property of lossy dielectric gives a banded submatrix for the Green's function of the lossy dielectric. The second property allows us, when using the free-space Green's function on the dense grid, to first average the values of surface unknowns on the dense grid and then place them on the sparse grid. PBTG speeds up the CPU and yet preserves the accuracy of the solution. It needs to be mentioned the PBTG is different from multigrid method. The multigrid method [10], [22] tries to facilitate the convergence of iteration in iterative techniques. It entails discretization of the structure into various grid sizes. The coarse grid corresponds to the low-frequency portion of the solution while the fine grid corresponds to that of the high-frequency solution. An iterative solution is obtained for each level of discretization and the solutions are interpolated from the coarse grid to the fine grid. The solution is first obtained in the coarse grid and then one moves to the next level of fine grid. Once the iterative solution is obtained in the fine grid, then one has to go back to the coarse grid to refine the solution. The present method that we have is based on scattering physics. The purpose of PBTG is to speed up the matrix-vector product of two Green's functions convolving with the surface fields on the dense grid.

In the previous paper [21], we developed PBTG for TE case. In this paper, we 1) combine the PBTG method with the BMIA/CAG method for improving of CPU and memory requirements; 2) study bistatic scattering coefficients and emissivity for TM case and compare TM and TE results; and 3) apply to low grazing scattering. We use it to treat a rough surface with a large surface length since the edge effects have to be avoided for low-grazing angle incidence [17], [20]. We use two grids, a dense grid and a coarse grid. The interaction is divided into (1) very near field of less than one wavelength, (2) near field of between one wavelength and r_d wavelengths, and (3) nonnear field beyond r_d wavelengths. In numerical simulations, r_d is an adjustable parameter so that BMIA/CAG can be used to solve the equations. In this paper, r_d is fixed at ten wavelengths. For very near-field interactions, we use a dense grid which is represented by four banded submatrics. For near-field and nonnear field interactions, the free-space Green's function is slowly varying on the dense grid. We can first average the fields on the dense grid to get fields on the sparse grid. The nonnear field interactions are also expanded on a canonical grid of a horizontal surface so that the fast Fourier transform (FFT) can be applied. In the lower medium, nonnear field interactions were neglected because of lossy properties of the lower medium. The approach is denoted as PBTG-BMIA/CAG. The computational complexity and the memory requirements for present algorithm are $O(N\log(N))$ and $O(N)$, respectively, where N is the number of surface unknowns on the coarse grid. Using this approach, we illustrate numerical results of TE and TM wave scattering up to surface length of 500 wavelengths and 30 000 surface unknowns. Note that all the surface unknowns on the dense grid are calculated by this method. The salient features of the numerical results are as follows.

(1) An SCG has poorer accuracy for TM case than for TE case.
(2) PBTG-BMIA/CAG speeds up CPU and preserves the accuracy. It has accuracy comparable to single dense grid and yet has CPU comparable to single coarse grid. It also gives surface fields on the dense grid and can give accurate results of the surface fields when the surface fields have rapid spatial variation.
(3) PBTG-BMIA/CAG gives accurate results for emissivity calculations and also for low-grazing backscattering problems (LGBA).

Thus PBTG-BMIA/CAG produces accurate results on the dense grid at CPU comparable with that of a single coarse grid.

In Section II, the formulation of the problem of TE and TM wave impinging upon a dielectric surface is given in terms of integral equations. Then the integral equations are converted into a matrix equation using a single-grid discretization. In Section III, we implement the physics-based two-grid algorithm and combine it with the BMIA/CAG method. In Section IV, the bistatic scattering coefficients and the emissivity are defined. In Section V, the numerical results are illustrated.

II. Formulation and Single Grid Implementation

Consider a tapered plane wave $\psi_{\rm inc}(x,z)$ with a time dependence of $e^{-i\omega t}$, impinging upon a 1-D rough surface with a random height profile $z=f(x)$. It is tapered so that the illuminated rough surface can be confined to surface length L [19]. The incident wave is

$$\psi_{\rm inc}(x,f(x))=\frac{g}{2\sqrt{\pi}}\int_{-\infty}^{\infty}dk_x e^{i(k_x x-k_z z)}e^{-\frac{(k_x-k_{ix})^2g^2}{4}} \tag{1}$$

where $k_{ix}=k\sin\theta_i$, $k_z^2=k^2-k_x^2$ with a proper choice of the branch cut, k is the wavenumber of the free-space, and g is the parameter that controls the tapering of the incident wave. Let ψ and ψ_1 denote, respectively, the wave functions for the upper medium and lower medium. They satisfy the following

surface integral equations [23]:

$$\frac{1}{2}\psi(\bar{r}') - \int_s \left[\psi(\bar{r})\frac{\partial G(\bar{r},\bar{r}')}{\partial \hat{n}} - G(\bar{r},\bar{r}')\frac{\partial \psi(\bar{r})}{\partial \hat{n}}\right] ds = \psi_{\text{inc}}(\bar{r}') \tag{2}$$

$$\frac{1}{2}\psi_1(\bar{r}') + \int_s \left[\psi_1(\bar{r})\frac{\partial G_1(\bar{r},\bar{r}')}{\partial \hat{n}} - G_1(\bar{r},\bar{r}')\frac{\partial \psi_1(\bar{r})}{\partial \hat{n}}\right] ds = 0 \tag{3}$$

where $\int_s$ denotes a Cauchy integral and G and G_1 are the two-dimensional (2-D) Green's function of the upper and lower medium that are given by

$$G(\bar{r},\bar{r}') = \frac{i}{4}H_0^{(1)}(k|\bar{r}-\bar{r}'|) \tag{4}$$

$$G_1(\bar{r},\bar{r}') = \frac{i}{4}H_0^{(1)}(k_1|\bar{r}-\bar{r}'|) \tag{5}$$

$H_0^{(1)}$ is the zeroth order Hankel function of the first kind and k_1 is the wavenumber of the lower medium. The wave functions Ψ and Ψ_1 are related through the boundary conditions on the surface S, namely,

$$\psi_1(\bar{r}) = \psi(\bar{r}) \quad \text{and} \quad \frac{\partial \psi_1(\bar{r})}{\partial \hat{n}} = \rho\frac{\partial \psi(\bar{r})}{\partial \hat{n}} \tag{6}$$

where ρ equals μ_1/μ and $\varepsilon_1/\varepsilon$ for TE and TM polarization, respectively. The integral equation is next discretized using an evenly spaced single grid. The surface is discretized into a single grid of N points for x between $-L/2$ and $L/2$ and the x_m points are at

$$x_m = (m-0.5)\Delta x - \frac{L}{2}, \quad m = 1,2,\cdots,N$$

$$\sum_{n=1}^{N} a_{mn}u(x_n) + \sum_{n=1}^{N} b_{mn}\psi(x_n) = \psi_{\text{inc}}(x_m) \tag{7}$$

$$\sum_{n=1}^{N} a_{mn}^{(1)}\rho u(x_n) + \sum_{n=1}^{N} b_{mn}^{(1)}\psi(x_n) = 0 \tag{8}$$

where $u(x) = \sqrt{1+[f'(x)]^2}\partial\psi/\partial n$. The matrix elements a_{mn}, b_{mn}, $a_{mn}^{(1)}$, and $b_{mn}^{(1)}$ are given by [16] (9)–(12), shown at the bottom of the page, where $r_{mn} = \sqrt{(x_n-x_m)^2+[f(x_n)-f(x_m)]^2}$ and $\gamma_m = \sqrt{1+[f'(x_m)]^2}$, $e = 2.718\,281\,83$, $H_1^{(1)}$ is the first-order Hankel function of the first kind, $f'(x_m)$ and $f''(x_m)$ represent the first and second derivative of $f(x)$ evaluated at x_m, respectively. The matrix equation in (7) and (8) is in the form of a single grid. Let $n = N/L$ be the number of points per wavelength. Usually a sample frequency of $n = 10$ is taken meaning that we have ten points per wavelength. We shall call such a sampling an SCG. If the sampling frequency is two or more times denser than the coarse grid, we shall call it an SDG. The dense grid that we use ranges from $n = 20$ to $n = 30$ in the paper.

III. Physics-Based Two-Grid Method Combined with Banded Matrix Iterative Approach/Canonical Grid Method

In this section, we describe the physics-based two-grid method correlated the BMIA/CAG.

Assume that the upper medium is the free-space and the lower medium is lossy with the following relative permittivity:

$$\varepsilon_1 = \varepsilon_1'(1 + i\tan\delta) \tag{13}$$

where $\tan\delta$ stands for loss tangent. Let λ and λ_1 represent the wavelength of the wave with the identical frequency in the free-space and the lower medium, respectively, and

$$n_1 = \text{integer}(\sqrt{\varepsilon_1'}). \tag{14}$$

Then, the relationship between λ and λ_1 can be expressed approximately by

$$\lambda_1 \approx \frac{\lambda}{n_1}. \tag{15}$$

The number of sampling points needed in the lower medium should be n_1 times more than that in the free-space.

In the physics-based two-grid method, we use two grids with samplings per wavelength of n_{cg} (coarse grid) and n_{dg} (dense grid), respectively. Let N_{dg} and N be, respectively, the

$$a_{mn} = \begin{cases} \Delta x\dfrac{i}{4}H_0^{(1)}(kr_{mn}) & m \neq n \\ \Delta x\dfrac{i}{4}H_0^{(1)}[k\Delta x\gamma_m/(2e)] & m = n \end{cases} \tag{9}$$

$$b_{mn} = \begin{cases} -\Delta x\dfrac{ik}{4}\dfrac{f'(x_n)(x_n-x_m)-[f(x_n)-f(x_m)]}{r_{mn}}H_1^{(1)}(kr_{mn}) & m \neq n \\ \dfrac{1}{2} - \dfrac{f''(x_m)}{4\pi}\dfrac{\Delta x}{\gamma_m^2} & m = n \end{cases} \tag{10}$$

$$a_{mn}^{(1)} = \begin{cases} -\Delta x\dfrac{i}{4}H_0^{(1)}(k_1r_{mn}) & m \neq n \\ -\Delta x\dfrac{i}{4}H_0^{(1)}[k_1\Delta x\gamma_m/(2e)] & m = n \end{cases} \tag{11}$$

$$b_{mn}^{(1)} = \begin{cases} \Delta x\dfrac{ik_1}{4}\dfrac{f'(x_n)(x_n-x_m)-[f(x_n)-f(x_m)]}{r_{mn}}H_1^{(1)}(k_1r_{mn}) & m \neq n \\ \dfrac{1}{2} + \dfrac{f''(x_m)}{4\pi}\dfrac{\Delta x}{\gamma_m^2} & m = n \end{cases} \tag{12}$$

total number of points on the dense grid and the coarse grid.

$$N_{\rm dg} = n_{\rm dg}\frac{L}{\lambda} \tag{16}$$

$$N = n_{\rm cg}\frac{L}{\lambda} \tag{17}$$

Usually $n_{\rm cg} = 10$ and $n_{\rm dg} = 10n_1$. We first rewrite (7) and (8) using the dense grid

$$\sum_{n=1}^{N_{\rm dg}} a_{mn}u(x_n) + \sum_{n=1}^{N_{\rm dg}} b_{mn}\psi(x_n) = \psi_{\rm inc}(x_m) \tag{18}$$

$$\sum_{n=1}^{N_{\rm dg}} a^{(1)}_{mn}\rho u(x_n) + \sum_{n=1}^{N_{\rm dg}} b^{(1)}_{mn}\psi(x_n) = 0. \tag{19}$$

The Roman numeral subscripts m, n denote indexing with the dense grid. Note that in the method of PBTG, the surface field at the dense grid are calculated. It is when the Green's function is multiplied with the surface fields on the dense grid, we can make substantial CPU saving by using PBTG. The matrix elements a_{mn}, b_{mn} represent Green's function of the upper medium while $a^{(1)}_{mn}, b^{(1)}_{mn}$ represents Green's function of the lower medium of the lossy dielectric. To reduce the calculation, we make the following three observations.

1) The Green's function in the lower region is heavily attenuative. A medium with a large real part of dielectric constant is normally associated with a large imaginary part. Let k_1'' be the imaginary part of k_1. If $k_1''r > C$, where C is a constant, then the field interaction between the mth and the nth point is vanishingly small. We can define a distance limit as dictated by dissipative loss

$$r_\ell = \frac{C}{k_1''} \tag{20}$$

outside of which the lower medium Green's function can be set equal to zero. The constant C depending on the loss tangent $\tan\delta$ varies from case to case. In this paper, C was fixed at 1.5.

Based on this observation, we calculate the left-hand sides of (19) as follows. We approximate

$$a^{(1)}_{mn} \approx \tilde{a}^{(1)}_{mn} = \begin{cases} a^{(1)}_{mn} & r_{mn} \le r_l \\ 0 & r_{mn} \ge r_l \end{cases} \tag{21}$$

$$b^{(1)}_{mn} \approx \tilde{b}^{(1)}_{mn} = \begin{cases} b^{(1)}_{mn} & r_{mn} \le r_l \\ 0 & r_{mn} \ge r_l \end{cases} \tag{22}$$

where r_{mn} is the distance between the mth point and the nth point on the dense grid. Thus, $\tilde{a}^{(1)}_{mn}$ and $\tilde{b}^{(1)}_{mn}$ are banded matrices and (19) becomes

$$\sum_{n=1}^{N_{\rm dg}} \tilde{a}^{(1)}_{mn}\rho u(x_n) + \sum_{n=1}^{N_{\rm dg}} \tilde{b}^{(1)}_{mn}\psi(x_n) = 0. \tag{23}$$

2) For nonnear field interaction, Green's function for the upper medium is slowly varying compared with Green's function of the lossy dielectric lower medium. Thus, when performing matrix and column-vector multiplication on the dense grid as indicated in (18), the Green's function of the upper medium is essentially constant over an interval of n_1 points on the dense grid. Thus, we can write

$$\sum_{l=1}^{n_1} a_{(m+l')(n+l)}u_{n+l} \approx a_{m_{\rm mp}n_{\rm mp}}\sum_{l=1}^{n_1} u_{n+l} = n_1 a_{m_{\rm mp}n_{\rm mp}}\left(\frac{1}{n_1}\sum_{l=1}^{n_1} u_{n+l}\right) \tag{24}$$

where $l' = 1, 2, \cdots, n_1$, and the points with indexes $m_{\rm mp}$ and $n_{\rm mp}$ are the middle points of the $(m+1)$th point and the $(m+n_1)$th point and the $(n+1)$th point and the $(n+n_1)$th point, respectively. What is done in (24) is that the surface fields on the dense grid are first averaged before multiplied by the upper medium Green's function.

3) The slowly varying nature of Green's function of the upper medium only applies to nonnear field interaction. For near field interaction, Green's functions G and G_1 have roughly the same rate of variation. Thus, we need to separate out a distance, say 1λ, outside of which G_1 is much more rapidly varying than G.

Based on the observations above, we decompose the upper medium Green's function into near field and nonnear field interactions

$$\sum_{n=1}^{N_{\rm dg}} a_{mn}u(x_n) = \sum_{n=1}^{N_{\rm dg}} a^s_{mn}u_n + \sum_{n=1}^{N_{\rm dg}} a^{ns}_{mn}u_n \tag{25}$$

$$\sum_{n=1}^{N_{\rm dg}} b_{mn}\psi(x_n) = \sum_{n=1}^{N_{\rm dg}} b^s_{mn}\psi_n + \sum_{n=1}^{N_{\rm dg}} b^{ns}_{mn}\psi_n \tag{26}$$

where a^s_{mn}, b^s_{mn}, a^{ns}_{mn}, and b^{ns}_{mn} are determined by

$$a^s_{mn} = \begin{cases} a_{mn} & r_{mn} \le r_f \\ 0 & r_{mn} \ge r_f \end{cases} \tag{27}$$

$$b^s_{mn} = \begin{cases} b_{mn} & r_{mn} \le r_f \\ 0 & r_{mn} \ge r_f \end{cases} \tag{28}$$

$$a^{ns}_{mn} = \begin{cases} 0 & r_{mn} \le r_f \\ a_{mn} & r_{mn} \ge r_f \end{cases} \tag{29}$$

$$b^{ns}_{mn} = \begin{cases} 0 & r_{mn} \le r_f \\ b_{mn} & r_{mn} \ge r_f \end{cases} \tag{30}$$

Thus, r_f is the distance outside which the Green's function of the lower medium is fast varying compared with that of free-space Green's function.

Let α and β denote the coarse grid indexes. The coarse grid has surface unknowns $\tilde{u}$ and $\tilde{\psi}$, which are averages of the dense grid surface unknowns. Thus, if $\bar{r}_\beta$ is centered in the middle of the n_1 dense grid points of $n+1, n+2, \cdots, n+n_1$, we have

$$\tilde{u}_\beta = \frac{u_{n+1} + u_{n+2} + \cdots + u_{n+n1}}{n_1} \tag{31}$$

$$\tilde{\psi}_\beta = \frac{\psi_{n+1} + \psi_{n+2} + \cdots + \psi_{n+n1}}{n_1}. \tag{32}$$

We calculate Green's function of the upper medium on the coarse grid. These are represented by $\tilde{a}_{\alpha\beta}$ and $\tilde{b}_{\alpha\beta}$ and (33)

and (34), shown at the bottom of the page, where $\Delta\tilde{x}$ is the coarse-grid sampling, $\Delta\tilde{x} = n_1\Delta x$, and Δx is the dense-grid sampling. Thus, (18) becomes

$$\left[\sum_{n=1}^{N_{\rm dg}} a_{mn}^s u(x_n) + \sum_{n=1}^{N_{\rm dg}} b_{mn}^s \psi(x_n)\right] + \left[\sum_{\beta=1}^{N} \tilde{a}_{\alpha\beta}\tilde{u}(x_\beta) + \sum_{\beta=1}^{N} \tilde{b}_{\alpha\beta}\tilde{\psi}(x_\beta)\right]_{\rm intp} = \psi_{\rm inc}(x_m). \tag{35}$$

Note in (35) that $\sum_{n=1}^{N_{\rm dg}} a_{mn}^s u(x_n)$ includes $N_{\rm dg}$ values of $m = 1, 2, \cdots, N_{\rm dg}$, while $\sum_{\beta=1}^{N} \tilde{a}_{\alpha\beta}\tilde{u}(x_\beta)$ only has N values of $\alpha = 1, 2, \cdots, N$. Thus, we first compute $\sum_{\beta=1}^{N} \tilde{a}_{\alpha\beta}\tilde{u}(x_\beta)$. Then we use linear interpolation to find $N_{\rm dg}$ on the dense grid. In (35), we use subscript intp to represent that interpolation.

In the original PBTG, the BMIA is used to solve matrix (23) and (35). In this paper, we use BMIA/CAG to solve matrix equation. We further divide nonnear field interactions into two regions which are separated by r_d. For the interactions between r_f and r_d, we implement matrix and vector multiplication directly. For the interactions larger than r_d, we expand $\tilde{a}_{\alpha\beta}$ and $\tilde{b}_{\alpha\beta}$ in Taylor series as in the BMIA/CAG so that the FFT's can be used to compute this part of the matrix-vector multiplication. The Taylor series expansion is given below:

$$H\big(k\sqrt{x_d^2 + z_d^2}\big) = \sum_{m=0}^{M} a_m(x_d)\left(\frac{z_d}{x_d}\right)^{2m}. \tag{36}$$

Here, $H(k\sqrt{x_d^2+z_d^2})$ represents both $H_0^{(1)}(k\sqrt{x_d^2+z_d^2})$ and $\frac{H_1^{(1)}(k\sqrt{x_d^2+z_d^2})}{\sqrt{x_d^2+z_d^2}}$, $x_d = (x - x')$, and $z_d = (z - z') = f(x) - f(x')$. The first three terms of the expansion coefficients are given in [19].

The accuracy of Taylor series expansion depends on the ratio of z_d/x_d, which, in turn, dictates the bandwidth of the stored near-field interactions.

IV. Bistatic Scattering Coefficient and Emissivity

After the matrix equation is solved, the surface field can be calculated. The bistatic scattering coefficient $\sigma(\theta_s, \theta_i)$ is a measure of the scattering from incident angle θ_i into scattered angle θ_s. It is defined by (37), shown at the bottom of the next page. In (37), $\alpha(\theta_s, x) = \sin\theta_s x + \cos\theta_s f(x)$ and $k_z = \sqrt{k^2 - k_x^2}$. The bistatic scattering coefficient has been normalized by the incident power impinging upon the rough surface. For scattering by a perfect conducting surface, the energy conservation test is that $\int \sigma(\theta_s, \theta_i)\, d\theta_s = 1$. For scattering by a dielectric surface, the emissivity of the rough surface at incident angle θ_i is

$$e(\theta_i) = 1 - \int d\theta_s \sigma(\theta_s, \theta_i). \tag{38}$$

Thus, emissivity is a measure of energy conservation in a scattering calculation. Because of reciprocity, emissivity is the same as absorptivity which is the amount of power absorbed

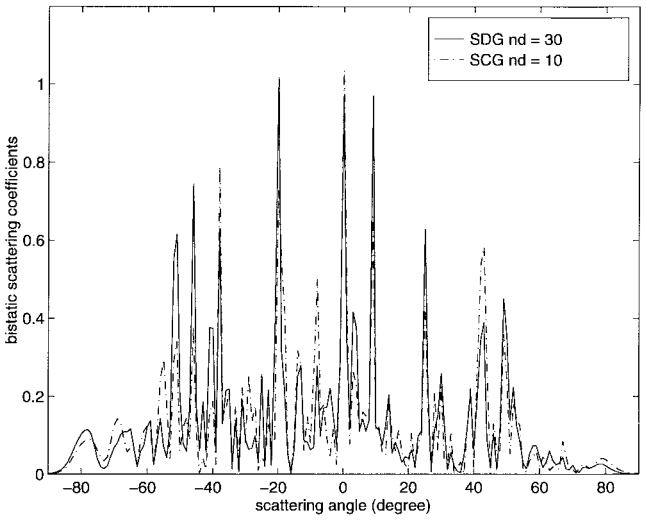

(a)

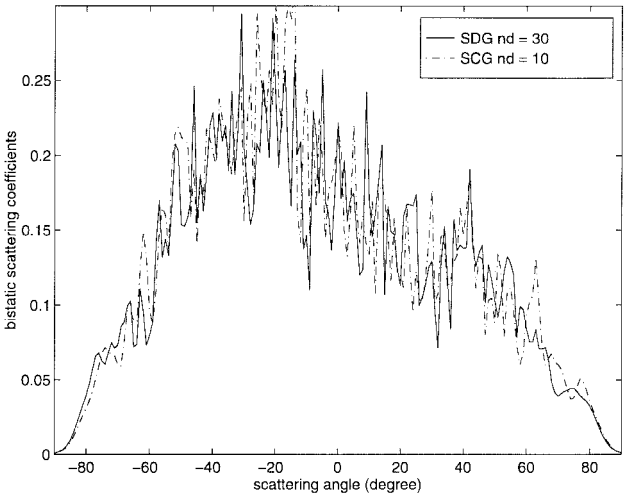

(b)

Fig. 1. Comparison of the bistatic scattering coefficients between the single dense grid of 30 points per wavelength and the single coarse grid of ten points per wavelength. TE wave, root mean square (rms) $h = 0.5\lambda$, correlation length of $l = 0.6\lambda$, dielectric constant of $\varepsilon_r = 25 + i$, surface length of $L = 100\lambda$, and tapering parameter of $g = L/4$ at incidence angle of $\theta_i = 30^\circ$. (a) One realization. (b) Twenty realizations.

$$\tilde{a}_{\alpha\beta} = \begin{cases} \Delta\tilde{x}\dfrac{i}{4}H_0^{(1)}(kr_{\alpha\beta}) & r_{\alpha\beta} > r_f \\ 0 & r_{\alpha\beta} \le r_f \end{cases} \tag{33}$$

$$\tilde{b}_{\alpha\beta} = \begin{cases} -\Delta\tilde{x}\dfrac{ik}{4}\dfrac{f'(x_\beta)(x_\beta - x_\alpha) - [f(x_\beta) - f(x_\alpha)]}{r_{\alpha\beta}}H_1^{(1)}(kr_{\alpha\beta}) & r_{\alpha\beta} > r_f \\ 0 & r_{\alpha\beta} \le r_f \end{cases} \tag{34}$$

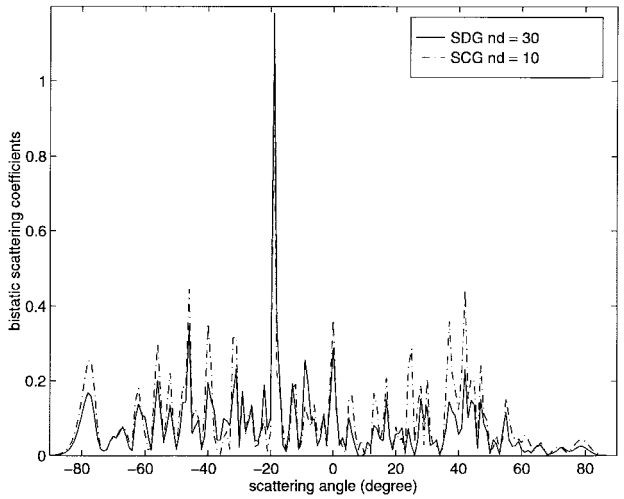

(a)

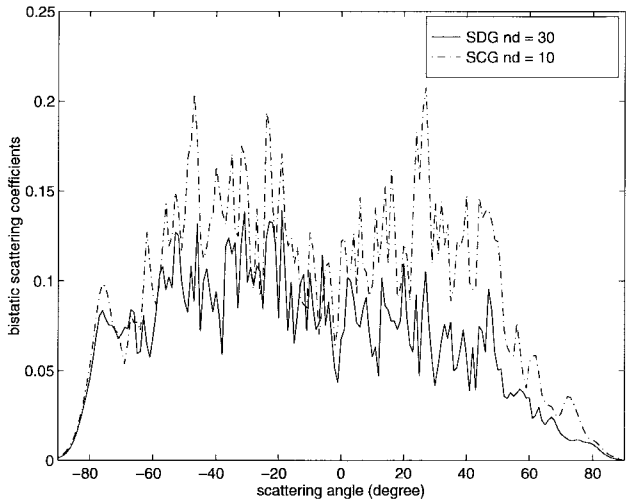

(b)

Fig. 2. Comparison of the bistatic scattering coefficients between the single dense grid of 30 points per wavelength and the single coarse grid of ten points per wavelength. TM wave, rms $h = 0.5\lambda$, correlation length of $l = 0.6\lambda$, dielectric constant of $\varepsilon_r = 25 + i$, surface length of $L = 100\lambda$, and tapering parameter of $g = L/4$ at incidence angle of $\theta_i = 30°$. (a) One realization (b) Twenty realizations.

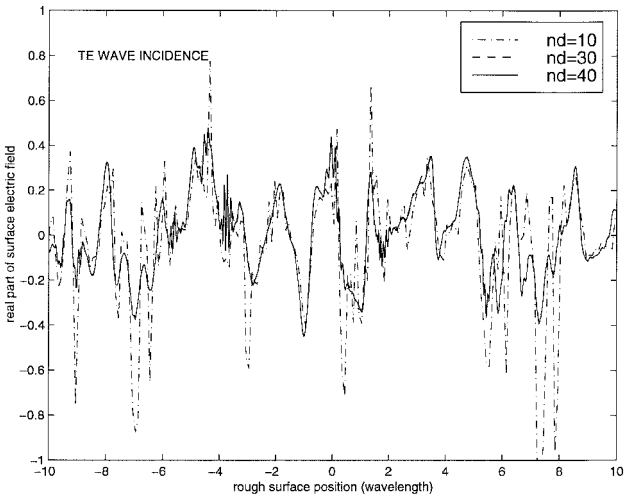

(a)

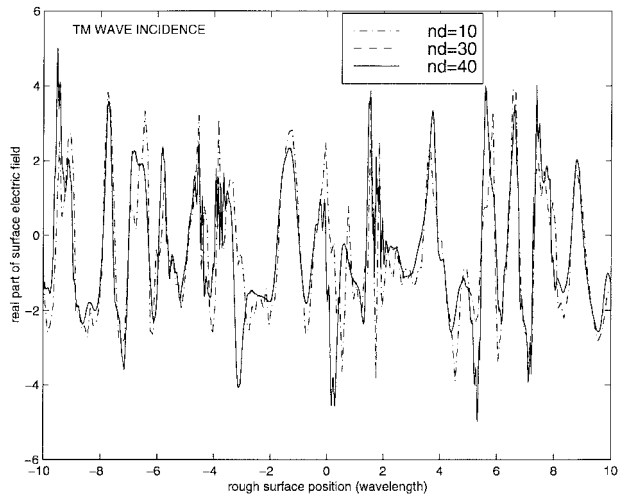

(b)

Fig. 3. Comparison of the surface fields between the single dense grid of 30 points per wavelength and the single coarse grid of ten points per wavelength rms $h = 0.5\lambda$, correlation length of $l = 0.6\lambda$, dielectric constant of $\varepsilon_r = 25 + i$, surface length of $L = 100\lambda$, and tapering parameter of $g = L/4$ at incidence angle of $\theta_i = 30°$. (a) TE wave. (b) TM wave.

by the dielectric in a scattering problem. In passive remote sensing, the brightness temperature T_B of the medium is measured at incident angle θ_i. The brightness temperature is

$$T_B(\theta_i) = e(\theta_i)T \tag{39}$$

where T is the physical temperature of the medium in Kelvin degrees. Brightness temperatures are commonly measured by instruments mounted on satellites and aircrafts. The brightness temperature can be measured to an accuracy of 1 °K. For the case of $T = 300$ K, an error of calculation in the emissivity of 0.03 gives an error of 9 K in brightness temperature and will not be acceptable. It is important that the scattering calculation obey energy conservation to less than 0.01, so that the error in brightness temperature is limited to less than 3 °K.

V. Numerical Results and Discussion

In this section, we illustrate the numerical simulation results of wave scattering from rough lossy dielectric surface for both TE and TM waves. Simulations are based on Gaussian random rough surfaces with Gaussian correlation functions. First, we show the comparisons of bistatic scattering coefficients and surface fields based on an SDG and an SCG with a dielectric constant of $25 + i$, surface length of 100 wavelengths and at

$$\sigma(\theta_s, \theta_i) = \frac{\left| \int_{-\infty}^{\infty} dx \left[ik\psi(x)\left(\frac{df}{dx}\sin\theta_s - \cos\theta_s\right) - u(x)\right] \exp(-ik\alpha(\theta_s, x)) \right|^2}{4\pi g^2 \int_{-k}^{k} dk_x k_z \exp[-(k_x - k\sin\theta_i)^2 g^2/2]} \tag{37}$$

TABLE I
COMPARISON OF EMISSIVITIES BASED ON PBTG-BMIA/CAG AND SINGLE GRID METHOD ($L = 100$ WAVELENGTH)

Method	n_d	Polarization	# of realization	Emissivity	difference of emissivity***
SCG*	10	TE	1	0.614097	+0.021753
SDG**	30	TE	1	0.592344	0
PBTG-BMIA/CAG	10 and 30	TE	1	0.602337	0.0099
SCG	10	TM	1	0.703530	-0.061699
SDG	30	TM	1	0.765229	0
PBTG-BMIA/CAG	10 and 30	TM	1	0.768926	0.003697
SCG	10	TE	20	0.592318	-0.013456
SDG	30	TE	20	0.605774	0
PBTG-BMIA/CAG	10 and 30	TE	20	0.613663	0.007889
SCG	10	TM	20	0.701566	-0.092587
SDG	30	TM	20	0.794153	0
PBTG-BMIA/CAG	10 and 30	TM	20	0.797086	-0.002933

SCG = Single Coarse Grid, SDG = Single Dense Grid, The difference of emissivity means the emissivity minus the emissivity of SDG.

TABLE II
COMPARISON OF CPU BASED ON PBTG-BMIA/CAG AND SINGLE GRID METHOD (1 REALIZATION AND $L = 100$ WAVELENGTH)

Method	n_d	# of surface unknowns	Polarization	CPU time (s) per iteration	# of iteration	CPU time(s)
SCG	10	2000	TE	14.5	416	6064.8
SDG	30	6000	TE	75.0	383	28757.0
PBTG-BMIA/CAG	10 and 30	6000	TE	11.6	662	7708.1
SCG	10	2000	TM	14.51	108	1595.0
SDG	30	6000	TM	77.0	108	8333.2
PBTG-BMIA/CAG	10 and 30	6000	TM	12.2	135	1655.0

an incidence angle of 30°. The results show that the dense grid is required for the case with large dielectric constant. We shall regard the SDG results to be correct. Next, we compare the results based on PBTG-BMIA/CAG with that of SDG. Then we use the new method to calculate the cases with large surface length at different incident angles and compare with SDG. Results indicate that the method still works well for large surface length and at near-grazing incidence angle. It is important to note that the PBTG-BMIA/CAG calculates the surface fields on the dense grid.

Our numerical results for rms heights less than a wavelength indicate that it requires a long surface to have accurate solutions of close to grazing incidence since the edge effects have to be avoided [17]. It has been reported that the surface length of 8192 wavelengths is needed for the incidence angle of 89° [20]. For the case of small incidence angle the required surface length can be much shorter. However, the advantage of the present method is for long surfaces and that is why the examples deal with cases with rms height less than a wavelength.

To avoid the edge effects, the tapering parameter was taken to $L/4$ be for the case of surface length of 100 wavelengths and $L/8$ for the case of surface length of 500 wavelengths at near-grazing incidence. The critical distance of r_f that defines the very near field is fixed at one wavelength in this paper. The cases with surface length of 100 wavelengths were run on SPARC 20 workstation and the cases with surface length of 500 wavelengths were run on Pentium-Pro Personal Computer with the clock rate of 200 MHz. The random rough surfaces used in the simulation are Gaussian random rough surfaces. The dielectric constant is set at $25 + i$.

A. Comparison Between Single Dense Grid and Single Coarse Grid

In Fig. 1(a) and (b), we compare, respectively, the results of the bistatic scattering coefficients of a single realization of rough surface and averaged over 20 realizations for TE wave, at incident angle $\theta_i = 30°$ and surface length $L = 100\lambda$, where λ is the wavelength. The rms height and correlation length are 0.5 and 0.6 wavelength, respectively. We compare the cases of SCG of $n_d = 10$ and SDG of 30 points per wavelength. We note that the results of SCG and SDG are quite different both for one realization and for averages over 20 realizations. Obviously, the results based on SCG are not accurate enough. The comparisons were also made in Fig. 2(a) and (b) for TM wave with the same parameters. It is noted that the performance of SCG is poorer for TM case. This is because the more energy is transmitted into the lower medium for TM case than for the TE case and the lower medium dielectric requires a dense discretization. In Fig. 3(a) and (b), we compare the surface electric fields between SDG and SCG for TE and TM waves, respectively. It is obvious that the coarse grid cannot give rapid spatial variation of the surface fields. In Table I, we compare the emissivities calculated for using one realization and 20 realizations for SCG and SDG for both TE and TM waves. We found that for SCG the emissivity is 0.614 097, while for SDG the emissivity is 0.592 344 for one realization of TE wave. The difference of emissivities of 0.021 753 can give a difference of $300\ \text{K} \times 0.021\,753 = 6.53\ \text{K}$ in brightness temperature. Even after averaging over 20 realizations, the emissivity for SCG still has $-0.013\,456$ difference from that of SDG. For TM wave, the difference of emissivity is much

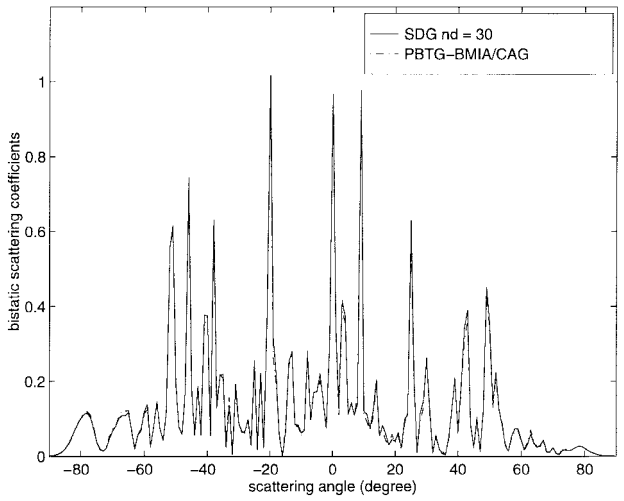

(a)

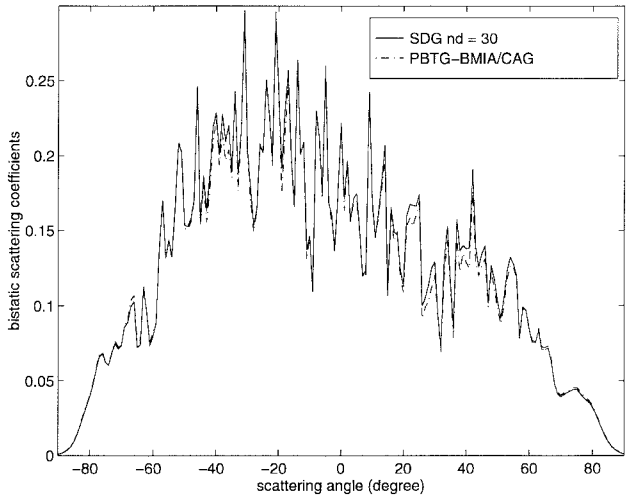

(b)

Fig. 4. Comparison of the bistatic scattering coefficients between the single dense grid of 30 points per wavelength and the PBTG-BMIA/CAG with $r_f = 1\lambda$. TE wave, rms $h = 0.5\lambda$, correlation length of $l = 0.6\lambda$, dielectric constant of $\varepsilon_r = 25 + i$, surface length of $L = 100\lambda$, and tapering parameter of $g = L/4$ at incidence angle of $\theta_i = 30^\circ$. (a) One realization (b) Twenty realizations.

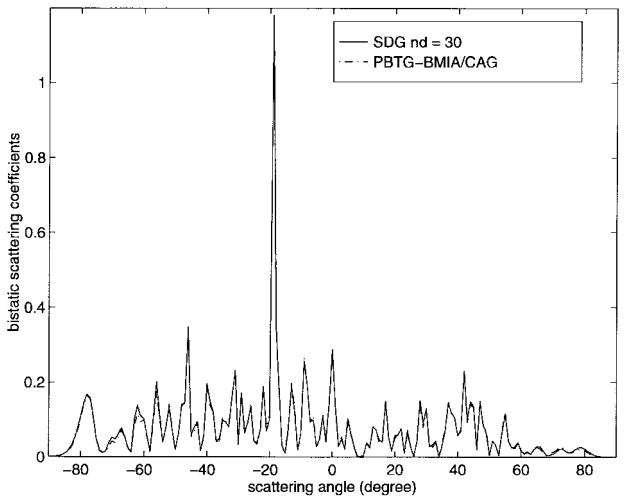

(a)

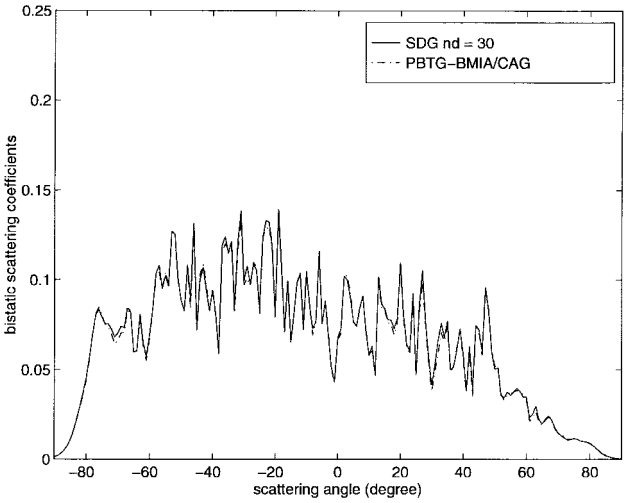

(b)

Fig. 5. Comparison of the bistatic scattering coefficients between the single dense grid of 30 points per wavelength and the PBTG-BMIA/CAG with $r_f = 1\lambda$. TM wave, rms $h = 0.5\lambda$, correlation length of $l = 0.6\lambda$, dielectric constant of $\varepsilon_r = 25 + i$, surface length of $L = 100\lambda$, and tapering parameter of $g = L/4$ at incidence angle of $\theta_i = 30^\circ$. (a) One realization (b) Twenty realizations.

larger. It is $-0.061\,699$ for one realization and $-0.092\,587$ for 20 realizations. This gives differences of 18.5 K and 27.78 K in brightness temperatures, respectively. Thus, SCG is not accurate for problems of large dielectric constant and cannot be used to calculate the emissivities. In Table II, we compare the CPU. We note that although SDG is accurate, it requires much more CPU than SCG. We regard the SDG results as accurate.

B. Comparison Between PBTG Combined with BMIA/CAG and Single Dense Grid

In Fig. 4(a) and (b), we compare the results of the bistatic scattering coefficients respectively obtained from a single realization of rough surface and averaged over 20 realizations of rough surfaces using SDG and PBTG-BMIA/CAG for TE wave. For PBTG-BMIA/CAG, the two grids are used with $n_{\rm cg} = 10$ and $n_{\rm dg} = 30$. The result obtained by PBTG-BMIA/CAG is almost identical to the SDG result. In Fig. 5(a) and (b), the comparisons are made for TM wave that also shows PBTG-BMIA/CAG can give almost the same results as SDG. The comparisons of the surface electric fields between SDG and PBTG-BMIA/CAG for TE and TM cases are shown in Fig. 6(a) and (b), respectively. The agreements are good since the PBTG-BMIA/CAG computes the surface fields on the dense grid. The emissivities calculated by SDG and PBTG-BMIA/CAG are compared in Table I. The emissivity calculated by PBTG-BMIA/CAG is very close to that of SDG for TE and TM waves. The difference of emissivities averaged over 20 realizations between SDG and PBTG-BMIA/CAG is $-0.007\,889$ for TE wave and $-0.002\,933$ for TM wave that will lead to maximum differences of 2.3667 K and 0.8799 K in brightness temperatures, respectively. We also compare the CPU between PBTG-BMIA/CAG, SDG, and SCG. In Table II, we give the comparisons of the total CPU and CPU per

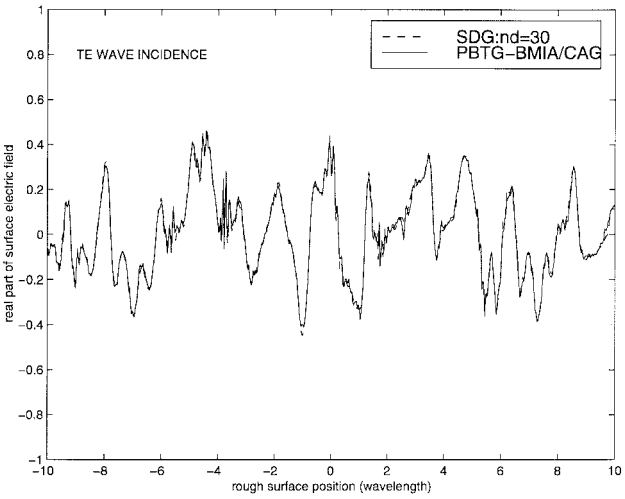

(a)

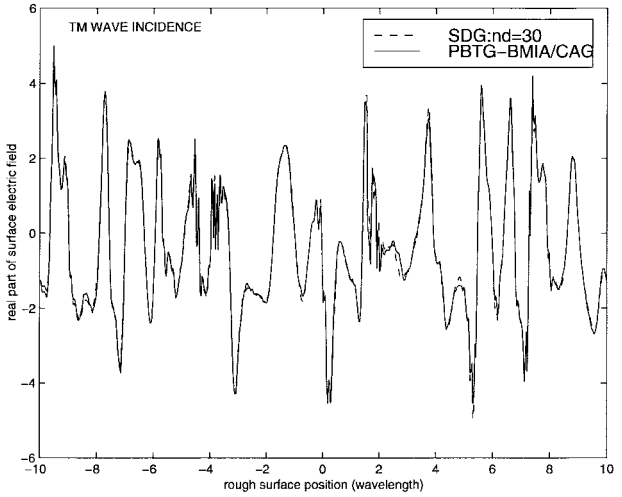

(b)

Fig. 6. Comparison of the surface fields between the single dense grid of 30 points per wavelength and the PBTG-BMIA/CAG with $r_f = 1\lambda$. rms $h = 0.5\lambda$, correlation length of $l = 0.6\lambda$, dielectric constant of $\varepsilon_r = 25 + i$, surface length of $L = 100\lambda$, and tapering parameter of $g = L/4$ at incidence angle of $\theta_i = 30°$. (a) TE wave. (b) TM wave.

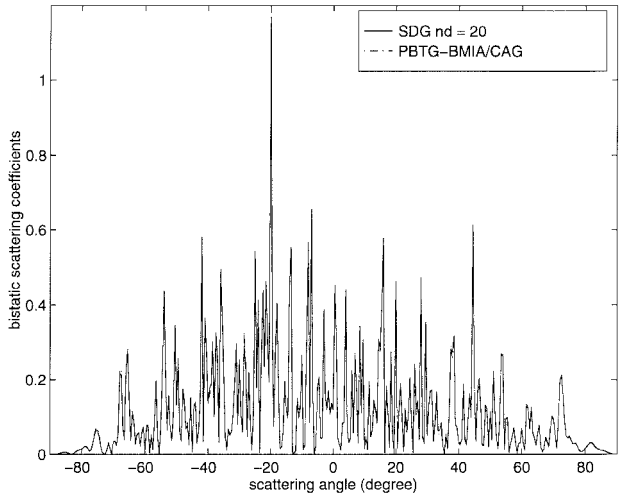

(a)

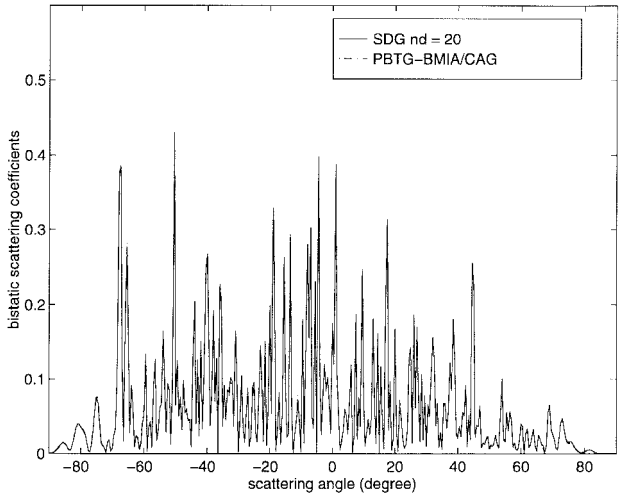

(b)

Fig. 7. Comparison of the bistatic scattering coefficients between the single dense grid of 20 points per wavelength and the PBTG-BMIA/CAG with $r_f = 1\lambda$ for one realization. rms $h = 0.3\lambda$, correlation length of $l = 0.5\lambda$, dielectric constant of $\varepsilon_r = 17 + i$, surface length of $L = 500\lambda$, and tapering parameter of $g = L/8$ at incidence angle of $\theta_i = 30°$. (a) TE wave. (b) TM wave.

iteration based on PBTG-BMIA/CAG and single grid methods for one realization. It is shown that the CPU per iteration is the smallest for PBTG and the largest for SDG. The total CPU of PBTG is slightly more than that of SCG because PBTG-BMIA/CAG requires more number of iterations. But the CPU of PBTG-BMIA/CAG is still several times less than that of SDG. The CPU for PBTG-BMIA/CAG is also comparable to SCG.

C. Comparison Between PBTG-BMIA/CAG and SDG for Large Surface Length Case

In Fig. 7(a) and (b), the bistatic scattering coefficients obtained by PBTG-BMIA/CAG and SDG, respectively, are compared for the case of a large surface length of 500 wavelengths, rms height of 0.3λ, correlation length of 0.5λ, and dielectric constant of $17 + i$ at incidence angle of 30° for one realization for both TE and TM waves. In this case, SDG has 20 points per wavelength. PBTG-BMIA/CAG is with $n_{\rm cg} = 10$ and $n_{\rm dg} = 20$. The agreements are good. The comparisons of emissivities and CPU are shown in Table III.

D. Backscattering Coefficients from Rough Surface with Large Dielectric Constant at Near-Grazing Incidence Angle

We also compare the bistatic scattering coefficients between PBTG-BMIA/CAG and SDG at incidence angle of 85° in Fig. 8(a) and (b). In this case, other parameters used are the same as the Figs. 7(a) and (b). The agreements are good except in the forward scattering directions. The agreement in the forward direction is reasonable. It is important to note that PBTG-BMIA/CAG gives accurate results in backscattering direction.

In Fig. 9(a), we show the bistatic scattering coefficients of TE wave at 85° incidence angle averaged over various number of realizations. In Fig. 9(b), we zoom in and show the bistatic scattering coefficients in the vicinity of backscattering

TABLE III
COMPARISON OF EMISSIVITY AND CPU BASED ON PBTG-BMIA/CAG AND SDG METHOD (1 REALIZATION AND $L = 500$ WAVELENGTH)

Method	# of surface unknowns	incident angle	Polarization	emissivity	CPU time (s) per iteration	# of iteration	CPU time(mins)
SDG	20000	30	TE	0.639483	42.87	792	566
PBTG-BMIA/CAG	20000	30	TE	0.645528	9.84	1579	259
SDG	20000	30	TM	0.803430	34.52	252	145
PBTG-BMIA/CAG	20000	30	TM	0.804980	9.57	326	52
SDG	20000	85	TE	0.140942	40.72	358	243
PBTG-BMIA/CAG	20000	85	TE	0.073925	9.23	604	93
SDG	20000	85	TM	0.508661	35.58	145	86
PBTG-BMIA/CAG	20000	85	TM	0.47590	9.83	183	30
PBTG-BMIA/CAG	30000	85	TE		13.1	1323	290
PBTG-BMIA/CAG	30000	85	TM		13.6	292	68

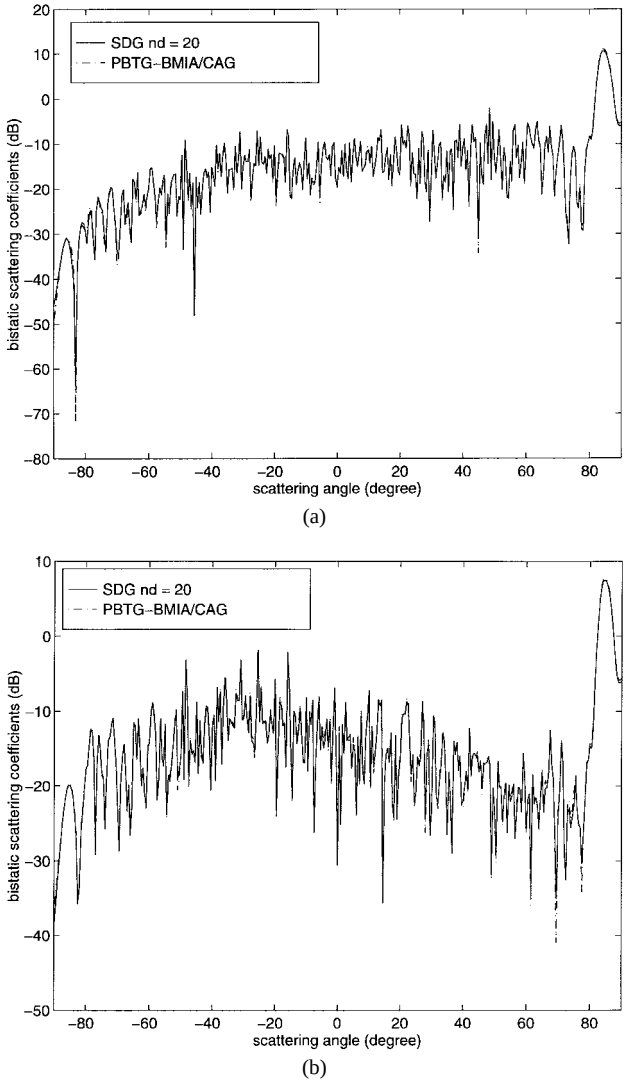

Fig. 8. Comparison of the bistatic scattering coefficients between the single dense grid of 20 points per wavelength and the PBTG-BMIA/CAG with $r_f = 1\lambda$ for one realization. rms $h = 0.3\lambda$, correlation length of $l = 0.5\lambda$, dielectric constant of $\varepsilon_r = 17 + i$, surface length of $L = 500\lambda$, and tapering parameter of $g = L/8$ at incidence angle of $\theta_i = 85°$. (a) TE wave. (b) TM wave.

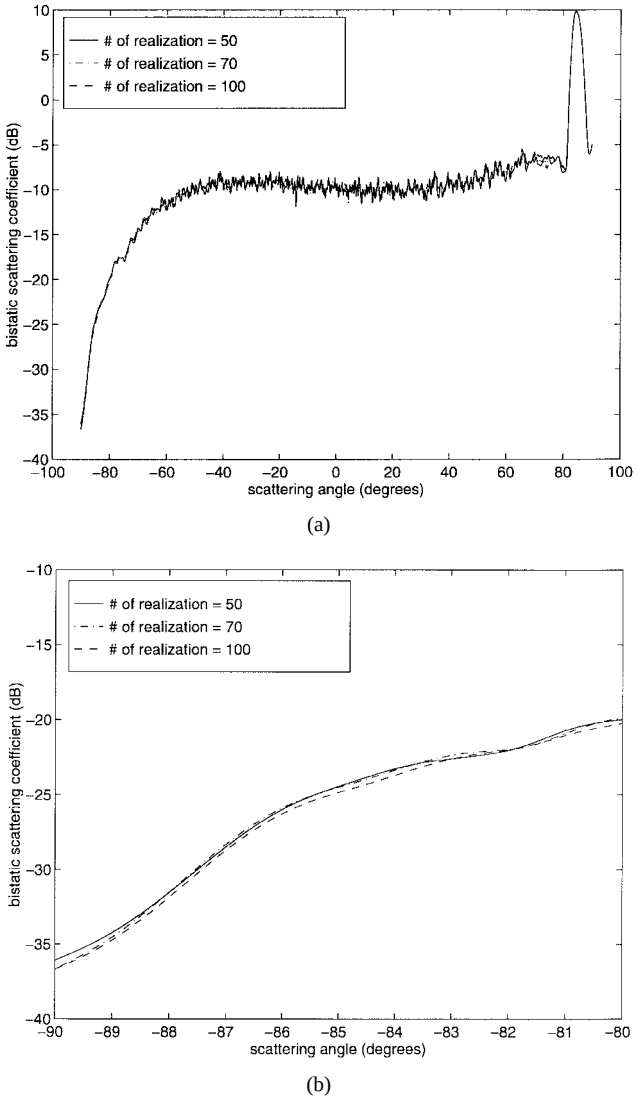

Fig. 9. Comparison of the bistatic scattering coefficients averaged over various number of realizations calculated by PBTG-BMIA/CG with $r_f = 1\lambda$ and using the dense grid of 30 points per wavelength and the coarse grid of 10 points per wavelength. TE wave, rms $h = 0.5\lambda$, correlation length of $l = 0.6\lambda$, dielectric constant of $\varepsilon_r = 25 + i$, surface length of $L = 500\lambda$, and tapering parameter of $g = L/8$ at incidence angle of $\theta_i = 85°$. (a) Entire range of scattering angles. (b) Vicinity of backscattering direction.

direction. In Fig. 10(a) and (b), we show the corresponding results for TM wave. We take the surface length of 500 wavelengths, rms height of 0.5λ, correlation length of 0.6λ, dielectric constant of $25 + i$. In PBTG-BMIA/CAG, we use two grids of ten points per wavelength and 30 points per wavelength. We did not calculate the results of SDG because of large CPU and memory requirements. We found that 50

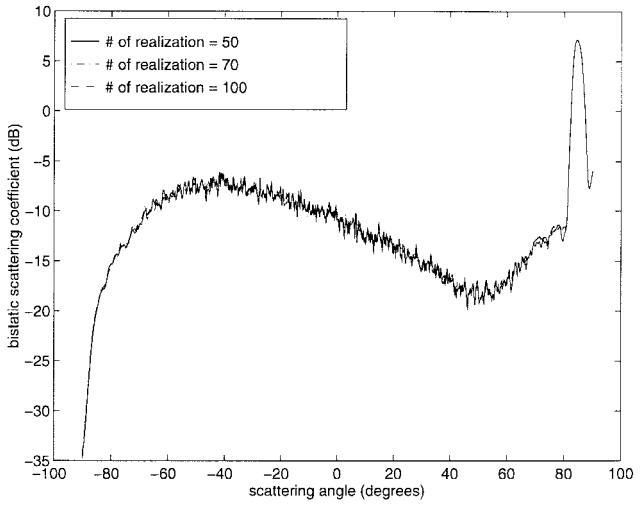

(a)

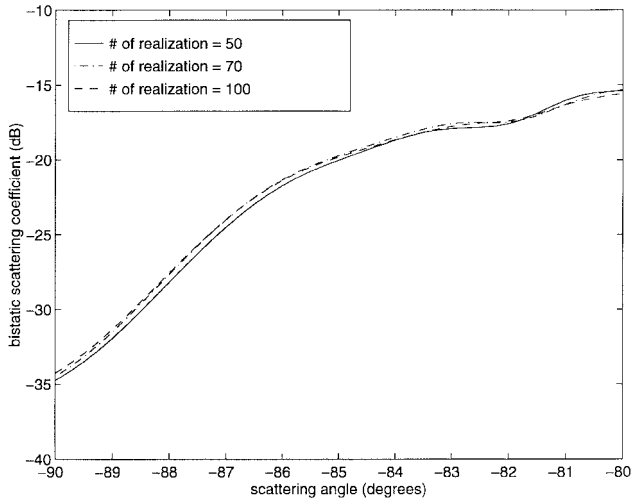

(b)

Fig. 10. Comparison of the bistatic scattering coefficients averaged over different realization number calculated by the PBTG-BMIA/CAG with $r_f = 1\lambda$ and using the dense grid of 30 points per wavelength and the coarse grid of ten points per wavelength. TM wave, rms $h = 0.5\lambda$, correlation length of $l = 0.6\lambda$, dielectric constant of $\varepsilon_r = 25 + i$, surface length of $L = 500\lambda$, and tapering parameter of $g = L/8$ at incidence angle of $\theta_i = 85°$. (a) Entire range of scattering angles. (b) Vicinity of backscattering direction.

realizations are required for convergence of backscattering coefficients for TE and 70 realizations are required for TM waves.

VI. Conclusion

In this paper, we have combined PBTG method with BMIA/CAG to calculate the wave scattering from rough surfaces of large surface length with a large lossy dielectric constant. The method saves both CPU and memory and provides the required accuracy. The computational complexity and the memory requirements of the present algorithm are $O(N\log(N))$ and $O(N)$, respectively, where N is the number of surface unknowns on the coarse grid. We also applied the method to calculate the backscattering coefficients from rough surface at near-grazing incidence angle and also the emissivities. The PBTG-BMIA/CAG gives accurate results when compared with SDG and with CPU time comparable with SCG. The method can be extended to the three-dimensional (3-D) case. Results for the 3-D case have been obtained and are being prepared for a separate publication.

References

[1] R. M. Axline and A. K. Fung, "Numerical computation of scattering from a perfectly conducting random surface," *IEEE Trans. Antennas Propagat.*, vol. AP-26, pp. 482–488, May 1978.

[2] A. A. Maradudin, E. R. Mendez, and T. Michel, "Backscattering effects in the elastic scattering of p-polarization light from a large amplitude random grating," in *Scattering in Volumes and Surfaces*, M. Nieto-Vesperians and J. C. Dainty, Eds. Amsterdam, The Netherlands: Elsevier, 1990.

[3] E. I. Thorsos, "The validity of the Kirchhoff approximation for rough surface scattering using a Gaussian roughness spectrum," *J. Acoust. Soc. Amer.*, vol. 83, pp. 78–92, 1988.

[4] J. S. Chen and A. Ishimaru, "Numerical simulation of the second order Kirchhoff approximation from very rough surfaces and study of backscattering enhancement," *J. Acoust. Soc. Amer.*, vol. 88, pp. 1846–1850, 1990.

[5] M. Nieto-Vesperinas and J. M. Soto-Crespo, "Monte-Carlo simulations for scattering of electromagnetic waves from perfectly conducting random rough surfaces," *Opt. Lett.*, vol. 12, pp. 979–981, 1987.

[6] C. Rino, T. Crystal, A. Koide, H. Ngo, and H. Guthart, "Numerical simulations of backscatterer from linear and nonlinear ocean surface realization," *Radio Sci.*, vol. 26, pp. 51–72, 1992.

[7] Y. Kim, E. Rodriguez, and S. Durden, "A numerical assessment of rough surface scattering theories: Vertical polarization," *Radio Sci.*, vol. 27, no. 4, pp. 515–527, July 1992.

[8] D. Maystre, M. Saillard, and J. Ingers, "Scattering by one- or two-dimensional randomly rough surfaces," *Waves Random Media*, vol. 1, pp. 143–155, 1991.

[9] R. Chen and J. C. West, "Analysis of scattering from rough surface at large incidence angles using a periodic-surface moment method," *IEEE Trans. Geosci. Remote Sensing*, vol. 33, pp. 1206–1213, Sept. 1995.

[10] D. J. Donohue, H. C. Ku, and D. R. Thompson, "Application of iterative moment-method solutions to ocean surface radar scattering," *IEEE Trans. Antennas Propagat*, vol. 46, pp. 121–132, Jan. 1998.

[11] V. Jandhyala, E. Michielssen, S. Balasubramaniam, and W. C. Chew, "A combined steepest descent-fast multipole algorithm for the fast analysis of three-dimensional scattering by rough surfaces," *IEEE Trans. Geosci. Remote Sensing*, vol. 36, pp. 738–748, May 1998.

[12] E. Michielssen, A. Boag, and W. C. Chew, "Scattering from elongated objects: Direct solution in $O(N\log^2 N)$ operations," *Proc. Inst. Elect. Eng.—Microwave Antennas Propagat.*, vol. 143, pp. 277–283, Aug. 1996.

[13] L. Tsang, C. H. Chan, and H. Sangani, "A banded matrix iterative approach to Monte Carlo simulations of scattering of waves by large-scale random rough surface problems: TM case," *Electron. Lett.*, vol. 29, no. 2, pp. 166–167, Jan. 1993.

[14] L. Tsang, C. H. Chan, H. Sangani, A. Ishimaru, and P. Phu, "A banded matrix iterative approach to Monte-Carlo simulations of large-scale random rough surface scattering: TE case," *J. Electromagn. Waves Applicat.*, vol. 7, no. 9, pp. 1185–1200, 1993.

[15] L. Tsang, C. H. Chan, K. Pak, and H. Sangani, "A BMIA/FFT algorithm for the Monte-Carlo simulations of large scale random rough surface scattering: Application to grazing incidence," in *IEEE Antennas Propagat. Soc. Int. Symp.*, Seattle, WA, June 1994, vol. 3, pp. 2028–2031.

[16] L. Li, C. H. Chan, and L. Tsang, "Numerical simulation of conical diffraction of tapered electromagnetic waves from random rough surfaces and applications to passive remote sensing," *Radio Sci.*, vol. 29, no. 3, pp. 587–598, May/June 1994.

[17] L. Tsang, C. H. Chan, K. Pak, and H. Sangani, "Monte-Carlo simulations of large-scale problems of random rough surface scattering and applications to grazing incidence with the BMIA/canonical grid method," *IEEE Trans. Antennas Propagat*, vol. 43, pp. 851–859, Aug. 1995.

[18] C. H. Chan, L. Li, and L. Tsang, "A banded matrix iteration approach to Monte Carlo simulation of large-scale random rough surface scattering: Penetrable case," in *Proc. 9th Annu. Rev. Progress Appl. Computat. Electromagn. Symp.*, Monterey, CA, Mar. 1993, pp. 391–397.

[19] C. H. Chan, L. Tsang, and Qin Li, "Monte-Carlo simulations of large-scale one-dimensional random rough surface scattering at near grazing incidence: Penetrable case," *IEEE Trans. Antennas Propagat.*, vol. 46, pp. 142–149, Jan. 1998.

[20] J. T. Johnson, "A numerical study of low-grazing angle backscatter from ocean-like impedance surfaces with the canonical grid method," *IEEE Trans. Antennas Propagat.*, vol. 46, pp. 114–120, Jan. 1998.
[21] L. Tsang and Qin Li, "Numerical solution of scattering of waves by lossy dielectric surfaces using a physics-based two-grid method," *Microwave Opt. Technol. Lett.*, vol. 16, no. 6, pp. 356–364, Dec. 20, 1997.
[22] W. L. Briggs, *A Multigrid Tutorial*. Philadelphia, PA: SIAM, 1987.
[23] L. Tsang, J. A. Kong, and R. T. Shin, *Theory of Microwave Remote Sensing*. New York: Wiley, 1985.

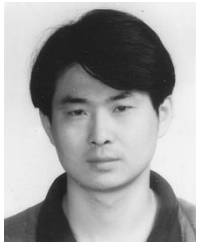

Qin Li received the B.S. and M.S. degrees in space physics in 1985 and 1988, respectively, from Wuhan University, China. He is currently working toward the Ph.D. degree in electrical engineering from the University of Washington, Seattle.

Chi Hou Chan (M'86) received the B.S. and M.S. degrees in electrical engineering from The Ohio State University, Columbus, in 1981 and 1982, respectively, and the Ph.D. degree in electrical engineering from the University of Illinois, Urbana, in 1987.

From 1987 to 1989, he was a Visiting Assistant Professor at the University of Illinois, associated with the Electromagnetic Communication Laboratory. He joined the Department of Electrical Engineering at the University of Washington, Seattle, in 1989 as an Assistant Professor. He was promoted to Associate Professor with tenure in 1993. Since April 1996, he has been with the Department of Electronic Engineering, City University of Hong Kong, where he is currently a Professor (Chair) of Electronic Engineering and Associate Dean of Faculty of Science and Engineering. His current research includes electronic packaging, remote sensing, antenna design and wireless communications.

Dr. Chan is a member of the U.S. URSI, Commission B and the recipient of the 1991 U.S. National Science Foundation Presidential Young Investigator Award. He is also a member of the Electromagnetic Academy and a fellow of the Institute of Electrical Engineers.

Leung Tsang (S'73–M'75–SM'85–F'90) was born in Hong Kong. He received the B.S. degree in 1971, the M.S. and E.E. degrees in 1973, and the Ph.D. degree in 1976, all from the Massachusetts Institute of Technology.

He is currently a Professor of electrical engineering at the University of Washington, Seattle. He was a Research Engineer at the Schlumberger-Doll Research Center from 1976 to 1978. From 1980 to 1983 he was with the Department of Electrical Engineering and Remote Sensing Center at Texas A&M University, College Station. He is a coauthor of *Theory of Microwave Remote Sensing* (New York: Wiley, 1985). He is on the editorial board of the *Journal of Electromagnetic Waves and Applications* and was an associate editor of *Radio Science*. His current research interests include wave propagation in random media and rough surfaces, remote sensing, and opto-electronics.

Dr. Tsang has been the editor of IEEE TRANSACTIONS ON GEOSCIENCE AND REMOTE SENSING since 1996. He was the Technical Program Chairman of the 1994 IEEE Antennas and Propagation International Symposium and URSI Radio Science Meeting, Technical Program Chairman of the 1995 Progress in Electromagnetics Research Symposium, and General Chairman of the 1998 IEEE International Geoscience and Remote Sensing Symposium. He is a fellow of the Optical Society of America.